Polymer 51 (2010) 1100–1110

Contents lists available at ScienceDirect

Polymer

journal homepage: www.elsevier.com/locate/polymer

Preparation and properties of polyurethane nanocomposites of novel architecture as advanced barrier materials

Pradip K. Maji [a], Nisith K. Das [b], Anil K. Bhowmick [a,*]

[a] Rubber Technology Centre, Indian Institute of Technology, Kharagpur 721302, India
[b] Variable Energy Cyclotron Centre, Dept. of Atomic Energy, Govt. of India, 1/AF, Bidhan Nagar, Kolkata 700064, India

ARTICLE INFO

Article history:
Received 25 September 2009
Received in revised form
15 December 2009
Accepted 29 December 2009
Available online 21 January 2010

Keywords:
Polyurethane
Permeability
Nanocomposite

ABSTRACT

The helium gas permeation through polyurethanes (PU) having novel microstructures derived from different polyols (varying from linear to hyperbranched) in the presence and absence of modified and unmodified nanoclays has been studied thoroughly in this paper. The permeation rate of helium gas decreases from linear to fourth generation polyols (PU_{40}) by about 80% due to increase in the crosslinking density. Similarly, the permeation rate of 8 wt% clay filled third generation hyperbranched PU dramatically decreases by about 76% in comparison to the unfilled PU. Gas-impermeable clay platelets in the PU matrix form tortuous pathways that further retard the progress of gas molecules. In addition, the well dispersed modified nanoclays contribute to improvement of the permeability properties to a great extent when compared with the aggregated unmodified ones. Further, interaction between the clays and the PU matrix plays a great role. Good correlation between dispersion of nanoclays in the PU matrix, as characterized by high resolution transmission electron microscopy and atomic force microscopy, and barrier resistance has been established. The permeation results have been compared with the different contemporary permeability models. The results are in line with the prediction by the Gusev-Lusti, the Nielsen and the Cussler (regular array) models at lower concentration of clay.

1. Introduction

Various polymeric films have been considered as a permeation barrier for gases such as helium, hydrogen and oxygen. Among the elastomers, polyurethane that can be used in space, defense, packaging and other applications has very low gas permeability [1]. Data on gas permeation of this material is, however, limited. Due to the rapid increase in its applications in different sectors especially in satellite mission, there is a current need for more experimental data which can be used to predict its performance and also a demand for polyurethane having unique microstructure to provide best barrier resistance. Therefore, it would be interesting to develop unique polyurethane networks, compare their barrier properties and establish a structure–property relationship. These networks are interesting because their morphological and physico–mechanical properties could be varied over a wide range by changing the chemical structure of constituents, their characteristics, and compatibility.

It is well known that permeation through a polymer depends on the nature of the polymer, degree of crystallinity, chain packing, chain stiffness, segment mobility and free volume [2–8]. In the past, most of the studies were concentrated on *linear* PUs [9–11]. Low cost hyperbranched (HB) dendritic polymers have received considerable and increasing attention in recent years [12,13]. The properties of dendritic polymers differ from their linear equivalents of the same molar mass, e.g. dendritic polymers exhibit lower viscosities, are non-entangled globular structures, and have higher solubilities in various solvents. It was shown recently that depending on the formulation, these networks could contain chemical clusters, making them very interesting to study the consequence of this nanostructure formation on the transport properties of the networks. The dendritic polymers having hydroxyl functionality can be a very useful member of the polyurethane family. Recently, we have developed different PUs with varying microstructures [14,15]. However, the structure-barrier resistance has not been explored. In this study, we have enhanced the gas barrier properties by using nanofillers. This is a part of our ongoing studies of structure–property relationship of various PU nanocomposites.

The hybrid organic–inorganic network morphology is often described as a dispersion of inorganic particles in an organic

* Corresponding author. Present address: Indian Institute of Technology, Patna 800013, India. Tel.: +91 3222 283180; fax: +91 3222 220312.
E-mail addresses: anilkb@rtc.iitkgp.ernet.in, director@iitp.ac.in (A.K. Bhowmick).

0032-3861/$ – see front matter © 2010 Elsevier Ltd. All rights reserved.
doi:10.1016/j.polymer.2009.12.040

thermoplastic or elastomeric matrix [16–18]. The basic question is whether the barrier resistance can be further improved through this philosophy. In the polymer literature, addition of nanofillers has been shown to improve barrier resistance [19,20]. Hence, an attempt has been made to understand the complex network.

The uniqueness of the present study is that crosslinked polyurethanes containing different microstructure and having distinctive nature of clay at different loadings have been successfully synthesized and characterized. Thus, the present study can help to reveal how the microstructure, nature of clay and clay loading affect the barrier properties of the polyurethane matrix.

A series of network in which polyurethane linear chains are connected by linear (here trimethylol propane) or by hyperbranched (HB) polyol (here 2nd, 3rd and 4th generation HB) crosslinker have been synthesized in bulk. The reaction scheme is given in Scheme 1. Amount of ingredients for the synthesis of stoichiometric system was calculated from the number of –OH groups in the crosslinker and –NCO groups present in the prepolymer. The detailed synthesis, characterization and evaluation of properties of PU and its nanocomposites have been described in the Experimental Section. Relationship between structure and barrier resistance has been discussed here in this paper.

2. Experimental

2.1. Materials

Poly(propylene glycol) (PPG), molecular weight 2000, was procured from Sigma–Aldrich Chemicals, Bangalore, India. Toluene-2, 4-diisocyanate (TDI) was purchased from Merck Schuchardt OHG, Hohenbrunn, Germany. Cloisite 30B containing 90 mequiv of quaternary ammonium ions/100 g of clay, Cloisite 15A, having 125 mequiv of quaternary ammonium ions/100 g of clay and Cloisite Na^+, were purchased from Southern Clay Products, Gonzales, TX, USA. The quaternary ammonium ion has a structure of $N^+(CH_2CH_2OH)_2(CH_3)T$, with T representing an alkyl group of approximately 65% C_{18}, 30% C_{16}, and 5% C_{14} for Cloisite 30B and the quaternary ammonium ion has a structure of $N^+(CH_3)_2(HT)_2$, where HT is hydrogenated tallow representing an alkyl group of approximately 65% C_{18}, 30% C_{16}, and 5% C_{14} for Cloisite 15A. Dibutyltin dilaurate (DBTL) was procured from Aldrich Chemicals, Bangalore, India. Dry solvent, tetrahydrofuran (THF), was purchased from Rankem, Kolkata, India. Second-generation (H20), third generation (H30), and fourth generation (H40) hyperbranched polyester polyol (Scheme 1) were procured from Perstorp Specialty Chemicals AB,

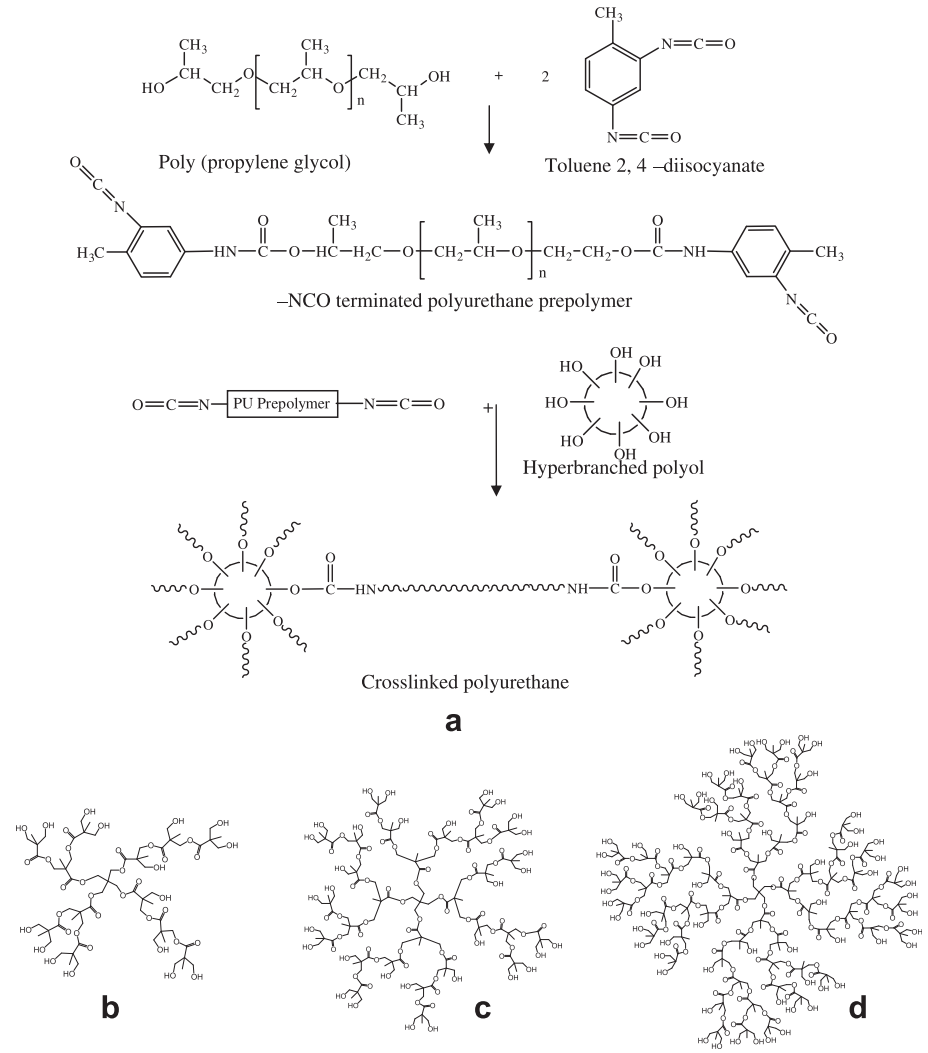

Scheme 1. (a) Reaction scheme of the crosslinking of polyurethane prepolymer with hyperbranched polyol; (b) Chemical structure of 2nd generation hyperbranched polyol; (c) Chemical structure of 3rd generation hyperbranched polyol; (d) Chemical structure of 4th generation hyperbranched polyol.

Perstorp, Sweden. Trimethylol propane (TMP) was procured from Merck, Mumbai, India.

2.2. Preparation of the PU prepolymer and PU nanocomposites

The PU prepolymer was synthesized in a nitrogen atmosphere by reacting 2 mol of TDI with 1 mol of PPG at 80 °C in a round-bottomed flask (500 cm^3) with continuous stirring. The exothermic reaction was controlled by cooling, and the temperature was maintained at 80 °C. The isocyanate (–NCO) concentration in the prepolymer reached a constant value after 4 h. The isocyanate content in the prepolymer was 4.4%, which was determined by the titrimetric method. The viscosity of the prepolymer determined by ASTM part 22D-1084 (1984) was found to be 2480 P. The molecular weight determined by the gel permeation chromatography (GPC) method was 2200 g/mol. The PU prepolymer was further characterized by Fourier transform infrared (FTIR) spectroscopy. The reaction scheme is shown in Scheme 1. The isocyanate-terminated PU prepolymer was characterized by a characteristic absorption peak at 2270 cm^{-1}. The peaks at 1730 and 3320 cm^{-1} also confirmed the development of the PU backbone in the PU prepolymer. The details of the reaction were given in our previous papers [14,15]. Proper precautions were taken during the handling of TDI because of its toxicity.

For the preparation of the nanocomposite, the prepolymer was reacted with three types of hyperbranched polyol materials (H20, H30, and H40) separately. An equivalent amount of branched polyol was added (equivalent ratio of –NCO:–OH = 1:1) to the diluted prepolymer in THF with constant stirring at room temperature (25 °C) in the presence of 0.001 mol of a DBTL catalyst. In order to investigate the effect of clay on the barrier property and the microstructure of the PU/clay nanocomposite, four concentrations of clay were used: 2.0, 4.0, 8.0, and 16.0 wt%. The clay was dispersed first in THF in a beaker by an ultrasonicator and finally added to the matrix with constant stirring. The samples for barrier property were prepared by casting of the solution in a circular quartz mold, and the thickness was adjusted by the amount of the cast solution. Neat PU was also synthesized by the same procedure without the addition of clay. The ratio of hard domain to the soft domain in resultant PU was 30:70.

2.3. Characterizations

2.3.1. FTIR spectroscopic studies

FTIR studies were carried out in dispersive mode on thin film samples (~100 μm) using a Perkin–Elmer FTIR spectrophotometer (model spectrum RX I), within a range of 400–4000 cm^{-1} using a resolution of 4 cm^{-1}. An average of 16 scans was reported for each sample.

2.3.2. Volume fraction of rubber in swollen gel and crosslinking density

Previously weighed samples were allowed to swell in THF at 30 °C for 48 h, the equilibrium swelling time (which was determined from a plot of mass uptake against time). The test pieces were then taken out, weighed and dried to a constant weight in a vacuum oven at 70 °C for 6 h. The volume fraction of the rubber in the swollen gel (V_r) was determined on the basis of simple additivity rule of volumes as follows (Eq. (1)):

$$V_r = \frac{(D - FH)/\rho_r}{(D - FH)/\rho_r + \rho_s} \quad (1)$$

where H = weight of the test specimen; D = deswollen weight of the test specimen; F = weight fraction of the insoluble components; A_o = weight of the absorbed solvent; ρ_r = density of the rubber; ρ_s = density of the solvent.

The apparent crosslinking density was calculated according to Flory–Rehner [21] (Eq. (2)) using the value of V_r as follows:

$$-\ln\left[(1 - V_r) + V_r + \chi \times V_r^2\right] = \frac{\rho}{M_c} \times V_s\left(V_r^{1/3} - \frac{V_r}{2}\right) \quad (2)$$

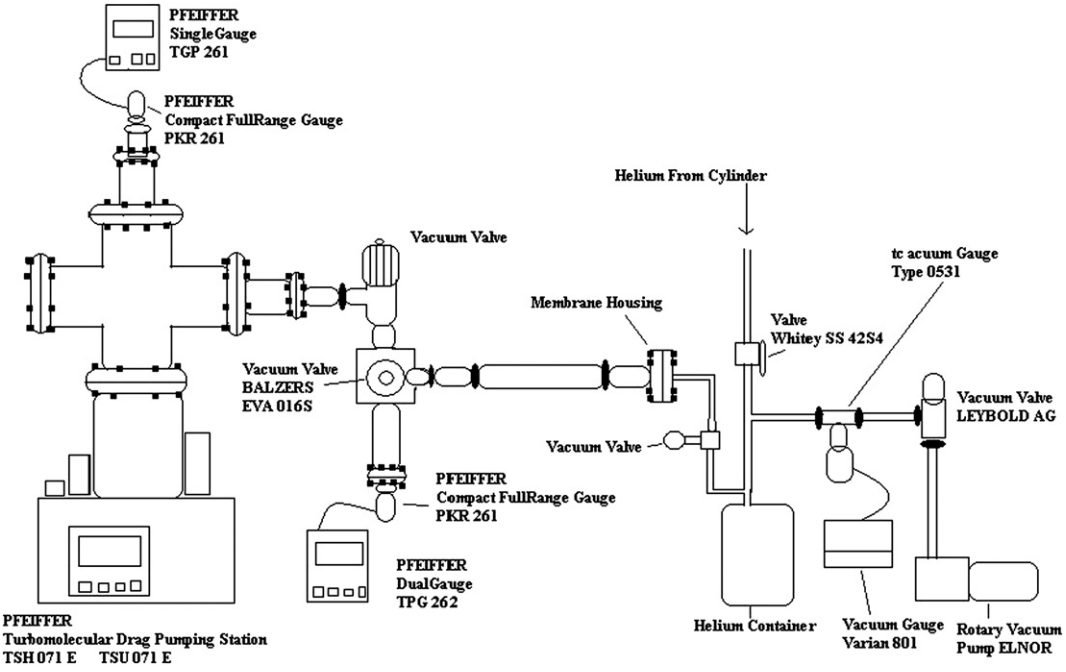

Fig. 1. Schematic diagram of helium gas permeation machine.

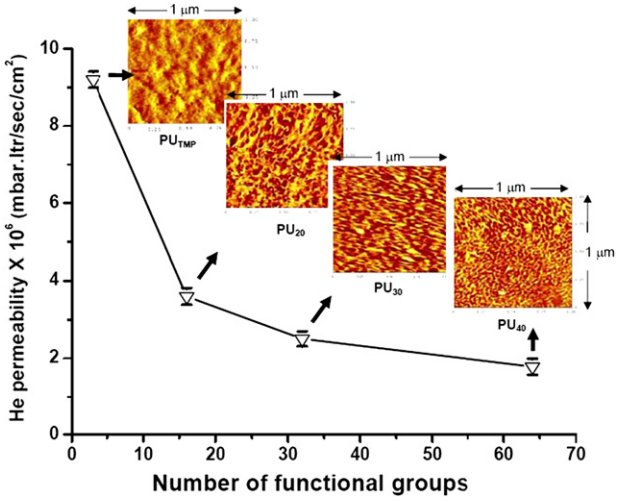

Fig. 2. Helium gas permeation rate of different polyurethanes. Permeability decreases with increase of the number of functional groups in the crosslinker molecules. There is a significant change in microstructure of different polyurethane cured by different crosslinker detected by Atomic Force Microscope. The error bar in this figure indicates standard deviation.

where χ = Flory–Huggins polymer–solvent interaction parameter; ρ = density of the rubber; M_c = molecular weight between crosslinks; V_s = molar volume of the solvent.

2.3.3. Transmission electron microscopy (TEM)

The samples for TEM analysis were prepared by ultracryomicrotomy with a Leica Ultracut UCT (Leica Mikrosystems GmbH, Vienna, Austria). Freshly sharpened glass knives with cutting edges of 45° were used to obtain cryosections of 50–70 nm thickness. Because these samples were elastomeric in nature, the sample and glass knife temperatures during ultracryomicrotomy were kept constant at −50 and −60 °C, respectively [these temperatures were well below the glass transition temperatures (T_g's) of PUs]. The cryosections were collected individually in a sucrose solution and directly supported on a copper grid of 300 meshes in size. Microscopy was performed with a JEOL JEM 2010 TEM instrument (Japan), operating at an accelerating voltage of 120 kV.

2.3.4. Atomic force microscopy (AFM)

Multi Mode Scanning Probe Microscope with a Nanoscope IIIa controller by Digital Instruments Inc. (Veeco Metrology Group), Santa Barbara, CA was used for the atomic force microscopy (AFM) studies. The AFM measurements of the ultramicrotomed (by Leica Ultracut UCT) surface of the cast cured polyurethane samples were carried out in air at ambient conditions (25 °C) using tapping mode probes with constant amplitude (40 mV). The rotated tapping mode etched silicone probe (RTESP) [square pyramid in shape with a spring constant of 20 N/m, nominal radius of curvature of 10 nm] with resonance frequency of 270 kHz was used. Phase images were recorded simultaneously at the resonance frequency of the cantilever with a scan rate of 1 Hz and a resolution of 256 samples per line. This allowed the resolution of individual primary block morphology measurements. The images were analyzed using a nanoscope image processing software (5.30r1).

2.3.5. Helium gas permeability measurement

Permeability testing was done using a device derived from the volumetric approach outlined in ASTM standard D1434 [22]. It was performed at 25 °C with a permeation cell attached to a helium detector. The peripheral devices are shown schematically in Fig. 1. Good vacuum-tight sealing was obtained with indium wires. The

Table 1
Volume fraction of rubber in the swollen gel (V_r) and crosslink density (M_c) of different polyurethanes and polyurethane nanocomposites by swelling experiment.

Sample designation	Clay loading (wt%)	V_r	M_c (g/mol)
PUTMP	0	0.154	9889
PU_{20} CB	0	0.157	5920
PU_{30}CB	0	0.193	4665
	2	0.199	4428
	4	0.207	4307
	8	0.209	4219
	16	0.231	3916
PU_{40}CB	0	0.200	3682
PU_{30}NA	8	0.194	4649
PU_{30}CA	8	0.195	4610

permeation measurement was made with helium as penetrant gas. A flat disc sample with a uniform thickness of 1.011–1.014 mm and surface area A (25 mm^2) separated a volume V_1 filled with gas under pressure p_1 from another volume V which was continuously evacuated. The gas leakage rate Q, derived from the difference Δp, was detected with a helium detector as a function of time, t, until a steady state was established and the permeation rate attained a saturation value Q_0. The permeability in terms of leak rate Q_0 was calculated from Eq. (3).

$$Q_0 = \frac{V \cdot \Delta p}{t \cdot A} \tag{3}$$

3. Results and discussion

3.1. Helium gas permeability of PU without nanofiller

Fig. 2 shows a plot of the experimentally determined helium gas permeability as a function of number of –OH functional groups of the crosslinker molecules. Permeability decreases significantly as crosslinker functionality is increased for a given microstructure, showing that nature of the crosslinker molecules plays a crucial role in determining the helium transport rate through the crosslinked polyurethane films. About four fold decrease in permeability occurs from trimethylol propane (having 3 –OH functional groups, PU_{TMP}) to 4th generation hyperbranched polyol (containing 64 –OH functional groups, PU_{40}) in the cured polyurethane, which arises partly due to change in microstructure, shown in the same figure. The origin of hilly lamellar structure of urethane component in the

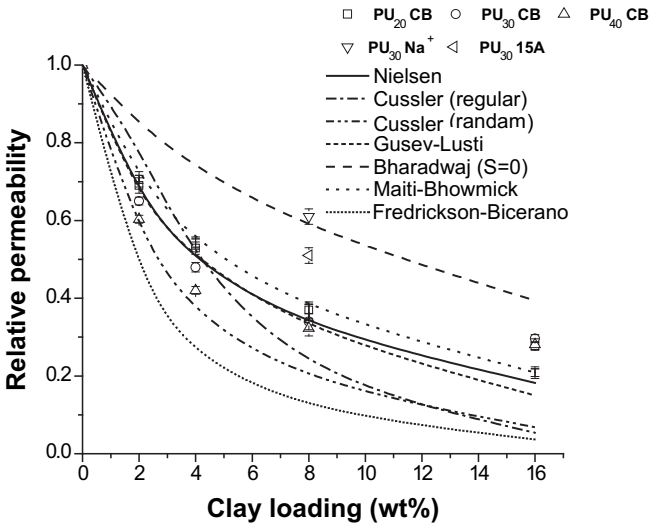

Fig. 3. Comparison between experimental data and model predictions for the relative permeability R_p in terms of level of nanoparticles loading. The error bar in this figure indicates standard deviation.

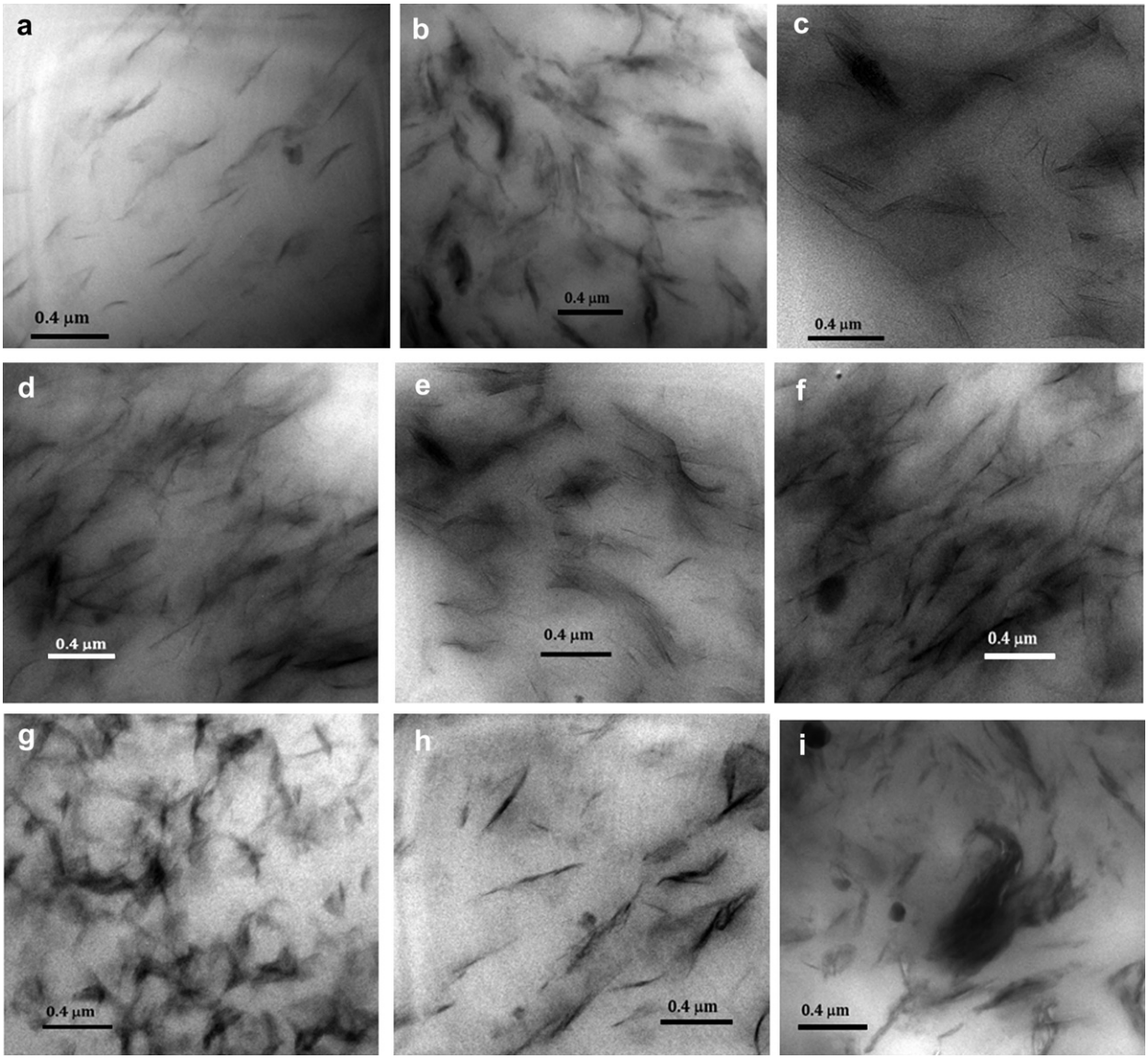

Fig. 4. Low magnification TEM photograph of different PUs at different clay loadings: (a) Polyurethane cured by 2nd generation hyperbranched polyol containing 2 wt% Cloisite 30B clay loading ($PU_{20}CB_2$); (b) Polyurethane cured by 2nd generation hyperbranched polyol containing 8 wt% Cloisite 30B clay loading ($PU_{20}CB_8$); (c) Polyurethane cured by 3rd generation hyperbranched polyol containing 4 wt% Cloisite 30B clay loading ($PU_{30}CB_4$); (d) Polyurethane cured by 3rd generation hyperbranched polyol containing 8 wt% Cloisite 30B clay loading ($PU_{30}CB_8$); (e) Polyurethane cured by 4th generation hyperbranched polyol containing 4 wt% Cloisite 30B clay loading ($PU_{40}CB_4$) (f) Polyurethane cured by 4th generation hyperbranched polyol containing 8 wt% Cloisite 30B clay loading ($PU_{40}CB_8$); (g) Polyurethane cured by 4th generation hyperbranched polyol containing 16 wt% Cloisite 30B clay loading ($PU_{40}CB_{16}$); (h) Polyurethane cured by 3rd generation hyperbranched polyol containing 8 wt% Cloisite Na^+ clay loading ($PU_{30}NA_8$); (i) Polyurethane cured by 3rd generation hyperbranched polyol containing 8 wt% Cloisite 15A clay loading ($PU_{30}CA_8$).

phase image from atomic force microscopy (AFM) is due to its higher surface energy than that of the softer polyether or polyester component. This lamellar morphology gives a domain width of 45–80, 30–50, 15–30, and 10–15 nm (calculated from the image analysis) for PU_{TMP}, PU_{20}, PU_{30} and PU_{40} respectively, for the hard urethane linkage. The separation of nanodomains is more distinct in the case of PU_{40} than that of PU_{20}, PU_{30} and PU_{TMP}. This explains that the formation of PU_{40} leads to the best dispersion of the hard domains in the final matrix, which is reflected in the gas permeation of this polyurethane. Our results correlating permeability to microstructure clearly support this view. Also, with an increase of number of functionality in the crosslinker molecules, more effective crosslinking occurs in the polyurethane network. The values of crosslinking densities of all the crosslinked PUs are tabulated in Table 1. With the increase of number of hydroxyl groups of the hyperbranched polyol, crosslink density increases in the PU matrix leading to decrease in M_c (shorter chains between the crosslinking points). PU_{TMP}, PU_{20}, PU_{30} and PU_{40} have M_c value of 9889, 5920, 4665 and 3682 g/mol respectively in the swelling experiment. The increment in crosslink density values with increase of number of functionality of the hyperbranched polyol can be attributed to the formation of urethane linkage between the molecules, which lead to a three dimensional network structure. Superior gas barrier property of PU_{40} is attributed to microphase-separated morphologies and higher crosslinking density due to presence of higher number of hydroxyl groups in 4th generation hyperbranched polyol (H40).

3.2. Helium gas permeability of PU with nanofiller

The addition of silicate layers into the above PUs could affect the gas diffusion mechanism through the material because of the

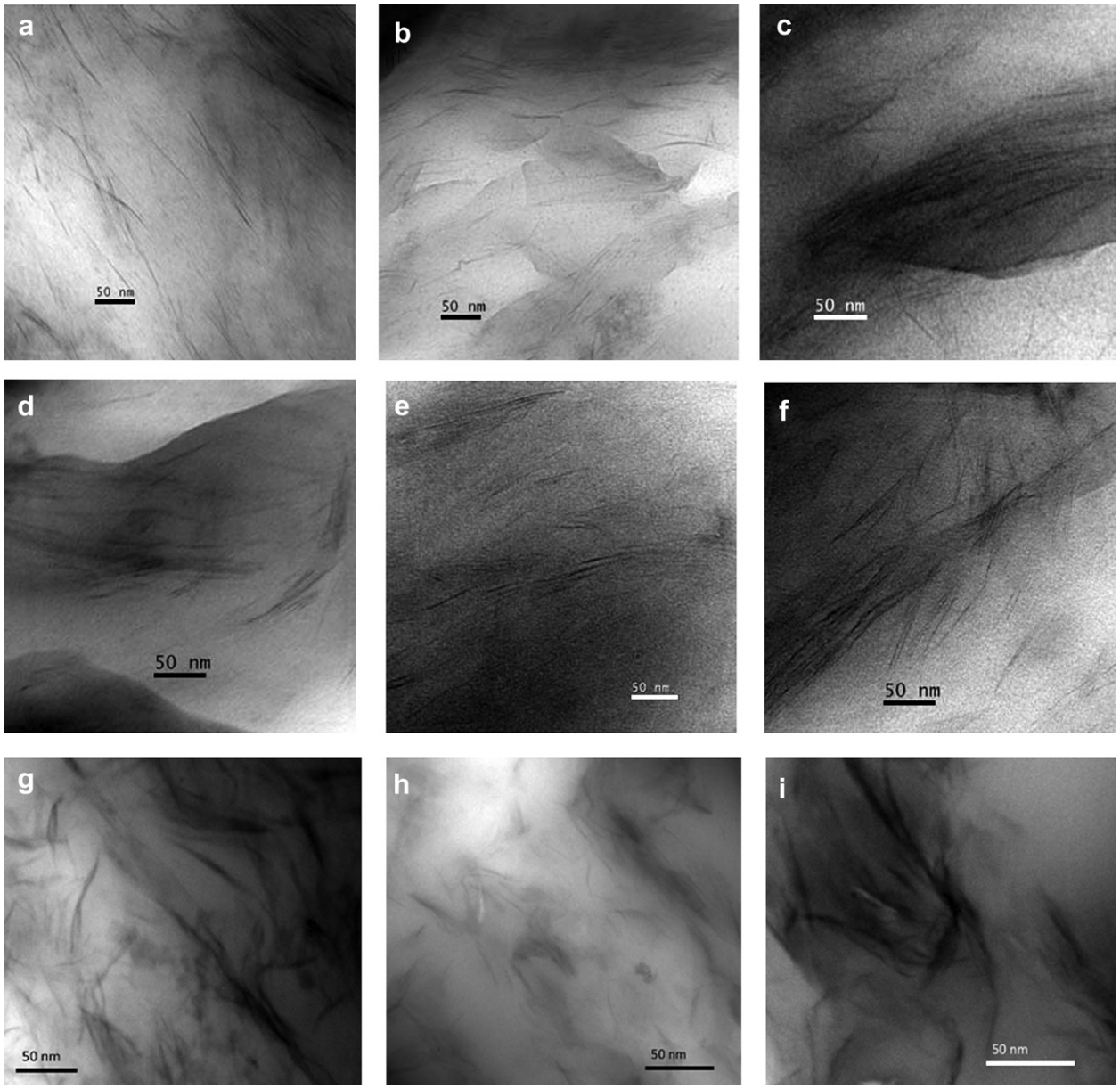

Fig. 5. High magnification of TEM photographs of different PUs at different clay loadings: (a) Polyurethane cured by 2nd generation hyperbranched polyol containing 2 wt% Cloisite 30B clay loading ($PU_{20}CB_2$); (b) Polyurethane cured by 2nd generation hyperbranched polyol containing 8 wt% Cloisite 30B clay loading ($PU_{20}CB_8$); (c) Polyurethane cured by 3rd generation hyperbranched polyol containing 4 wt% Cloisite 30B clay loading ($PU_{30}CB_4$); (d) Polyurethane cured by 3rd generation hyperbranched polyol containing 8 wt% Cloisite 30B clay loading ($PU_{30}CB_8$); (e) Polyurethane cured by 4th generation hyperbranched polyol containing 4 wt% Cloisite 30B clay loading ($PU_{40}CB_4$) (f) Polyurethane cured by 4th generation hyperbranched polyol containing 8 wt% Cloisite 30B clay loading ($PU_{40}CB_8$); (g) Polyurethane cured by 4th generation hyperbranched polyol containing 16 wt% Cloisite 30B clay loading ($PU_{40}CB_{16}$); (h) Polyurethane cured by 3rd generation hyperbranched polyol containing 8 wt% Cloisite Na^+ clay loading ($PU_{30}NA_8$); (i) Polyurethane cured by 3rd generation hyperbranched polyol containing 8 wt% Cloisite 15A clay loading ($PU_{30}CA_8$).

different permeability properties of the matrix and the inorganic particles. This phenomenon is particularly interesting when a filler of nanometric size is dispersed into the polyurethane matrix. It is observed that for the polyurethane matrix cured with third generation hyperbranched polyol (PU_{30}), the permeability of helium decreases with increase in clay (Cloisite 30B) concentration (Fig. 3). The composition containing 8 wt% of clay shows permeability reduction by about 76% over the pristine polyurethane; but beyond that, the decrease is not so significant (for 16 wt% loading, the reduction is 78%). The same trend of decrease of permeability for both PU_{20} and PU_{40} based nanocomposites is shown in Fig. 3. PU_{40} nanocomposites exhibit lowest permeability. In general, there are three reasons for enhancement of gas barrier property for polymer/clay nanocomposites. Firstly, gas-impermeable nanoclay layers dispersed in the polymer matrix form tortuous pathways, which retard the progress of gas molecules through the composite. Secondly, exfoliated clay layers and intercalated clay layer bundles strongly restrict the motion of the polymer chains, probably reducing the coefficient of diffusion of the gas molecules. Thirdly, the smaller M_c, (shorter chains between the crosslinking points) which increases crosslinking density due to reaction between the reacting groups in the nanoclay and the polymer, restricts the motion of the diffusion of the gas molecules. These are discussed below.

Images from low and high magnification transmission electron microscopy (TEM) and atomic force microscopy (AFM) give the

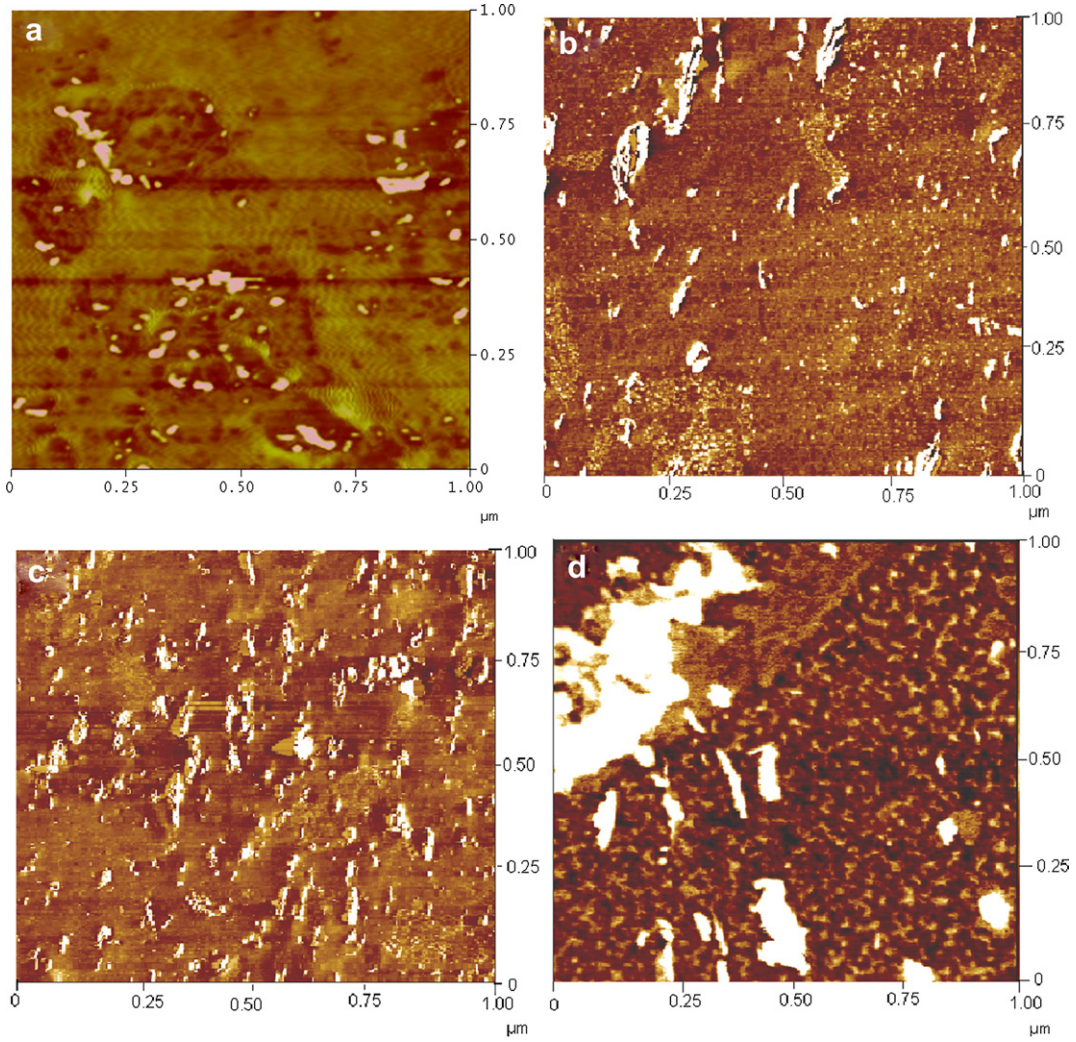

Fig. 6. AFM photograph of different PUs at different clay loadings: (a) Polyurethane cured by 2nd generation hyperbranched polyol containing 2 wt% Cloisite 30B clay loading ($PU_{20}CB_2$); (b) Polyurethane cured by 2nd generation hyperbranched polyol containing 4 wt% Cloisite 30B clay loading ($PU_{20}CB_4$); (c) Polyurethane cured by 3rd generation hyperbranched polyol containing 8 wt% Cloisite 30B clay loading ($PU_{30}CB_8$); (d) Polyurethane cured by 3rd generation hyperbranched polyol containing 8 wt% Cloisite Na^+ clay loading ($PU_{30}NA_8$).

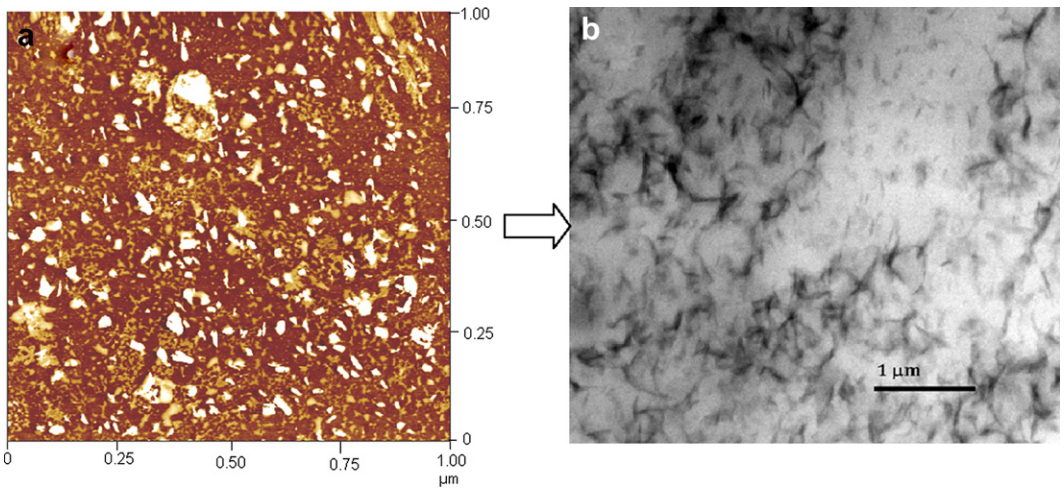

Fig. 7. Comparison of $PU_{40}CB_8$ (a) AFM image with that of (b) TEM photograph.

comprehensive insight of the dispersion of clay. The low magnification TEM images give the global dispersion of the clay in the matrix. Indeed, at low magnification TEM images (Fig. 4), the clays are seen to be randomly dispersed, with some intercalation of the platelets in the PU matrix up to 8 phr loading of Cloisite 30B clay. Clearly, the nanocomposite films exhibit the same morphological features as exfoliated or dispersed and intercalated throughout the PU matrix. This inference is supported by the higher magnification images (Fig. 5) which show well dispersed nanoclay platelets in the PU matrix up to 8 phr of Cloisite 30B loading. The gas transmission rate decreases slowly with increasing filler weight fraction. The reduction in transmission rate is obviously a consequence of the tortuous path the gas molecules has to cover during their random molecular motion in order to penetrate the composite film. It should be remarked that the nanoclay platelets are randomly oriented as observed in the TEM micrographs, which reduces their influence on the transmission rate. That is, a stronger reduction in the gas transmission rate can be expected with a better dispersion of nanoclay in the PU matrix. Better is the dispersion of clay, better will be the gas barrier property. Above 8 wt% of nanoclay, this levels off or slightly increases probably due to a decrease in exfoliation or collapse of the layers as the inter particle distance diminishes at higher concentration. The TEM micrographs show a homogeneous dispersion of silicate layers in the polymer matrix up to 8 wt% clay loading (Figs. 4b, d, f, and 5b, d, f). Figs. 4g and 5g exhibit the morphology of $PU_{40}CB_{16}$ filled with 16 wt% of organoclay loading. The image shows intercalation and agglomeration of silicate layers throughout the PU matrix instead of exfoliation.

Atomic force microscopy (AFM) has also been used to investigate the dispersion of clay from the fresh cut surface of bulk morphology of the neat PU and its clay nanocomposites. AFM phase images are provided in Figs. 6 and 7a. Phase images of the bulk of the samples (Figs. 6 and 7a) reveal different morphologies of the nanocomposites prepared. Examination of a number of samples of PU nanocomposites containing Cloisite 30B clay indicates bright white clay stacks in patches distributed in a mixed fashion with fine intercalation, as evident from Fig. 6a–c. Best exfoliation demonstrated by the nanocomposites containing 8 wt% of Cloisite 30B clay (Figs. 6b and 7a) indicates better interaction between the clay and the polymer in the nanocomposites. This is in line with TEM studies. When very high magnification of TEM image is compared with that of AFM image in Fig. 7, it is clear that at 8 wt% clay loading both the images depict the same trend of dispersion of clay in the PU matrix.

There is an enhancement in the crosslink density with increase of Cloisite 30B clay concentration in the polyurethane matrix. The crosslink density values are tabulated in Table 1. The M_c of $PU_{30}CB_0$ is 4668 g/mol, which decreases to 4219 g/mol when 8 wt% of Cloisite 30B is added. Superior gas barrier property of PU nanocomposites is also attributed to higher crosslinking leading to reduction in helium gas permeability.

The helium gas permeability of PU_{30} nanocomposites with 8 wt% clay loading obtained from different modified (Cloisite 30B, Cloisite 15A) and unmodified (Cloisite Na^+) clays can be compared. PU_{30} nanocomposites prepared from the modified clays show better gas barrier property over their unmodified counterpart (Fig. 3). The difference in permeability between the modified and the unmodified clay filled systems is considerably high, which indirectly proves that the dispersion of Cloisite Na^+ in PU_{30} matrix is poor. From the TEM micrograph (Figs. 4h and 5h), agglomeration of clay platelets is also observed in the case of PU_{30} nanocomposites containing 8 wt% Cloisite Na^+. AFM image of $PU_{30}NA_8$ also provides the same information. Fig. 6d delineates agglomerated clay structures with average size of approximately 600 nm in PU matrix. Among the modified clays, the nanocomposite containing Cloisite 30B clay gives the best barrier property. This is due to the fact that the modifier compound in Cloisite 30B contains –OH groups (from the typical structure $N^+(CH_2CH_2OH)_2(CH_3)T$, where T is the tallow) which have a strong tendency to interact with the –NCO group present in PU prepolymer. As a result, better dispersion (Figs. 4d and 5d) of clay platelets is achieved in the case of PU_{30} nanocomposites containing Cloisite 30B. There is no such interaction in PU_{30} nanocomposites containing Cloisite 15A (the modifier contains $N^+(CH_3)_2(HT)_2$, where HT is the hydrogenated tallow) (Figs. 4i and 5i). The agglomeration of clay is shown in the TEM images (Figs. 4h, i and 5h, i). Both Cliosite Na and 15A filled PU matrices have established its poor performances in the gas barrier property.

In order to investigate the interaction between the clay and the polymers, absorption peak at 2270 cm^{-1} of –NCO groups in the FTIR spectrum has been monitored. For this purpose, 5 g of prepolymer and 0.4 g of dried clay were mixed in the presence of 20 mL of dry THF by a magnetic stirrer at room temperature (25 °C) to produce a uniform mixture for about 2 h. A few drops of the prepolymer/clay mixture were taken in KBr disks and THF was allowed to evaporate for a period of 30 min. The clay/polymer reaction was followed by monitoring of the stretching of –NCO and C=O groups. A reduction of –NCO peak and increase of C=O peak intensity are observed in the case of Cloisite 30B clay (Fig. 8). There is no change in peak intensity when same procedure was followed with Cloisite 15A and Cloisite Na. The change in peak intensity is due to reaction between $–CH_2CH_2OH$ groups in Cloisite 30B clay and –NCO group of PU prepolymer leading to the urethane formation. It is worth noting that the organic ammonium ions, e.g., those present in Cloisite 30B, can potentially promote trimerization of –NCO groups [23]; however, this is not observed in the present study because the characteristic peaks at 1695–1715 cm^{-1} due to trimers of –NCO [24] do not appear during the course of the reactions. –NCO peaks do not disappear completely in a period of 120 min.

The reaction between the clay and polyurethane chains has also been characterized by monitoring the FTIR spectrum of the residue of the Soxhlet extraction of $PU_{30}CB_8$, $PU_{30}NA_8$ and $PU_{30}CA_8$. For this purpose, we have resorted to Soxhlet extraction of the composite materials to determine the amounts of residue as described in literature [25]. It is interesting to note that a trace amount of

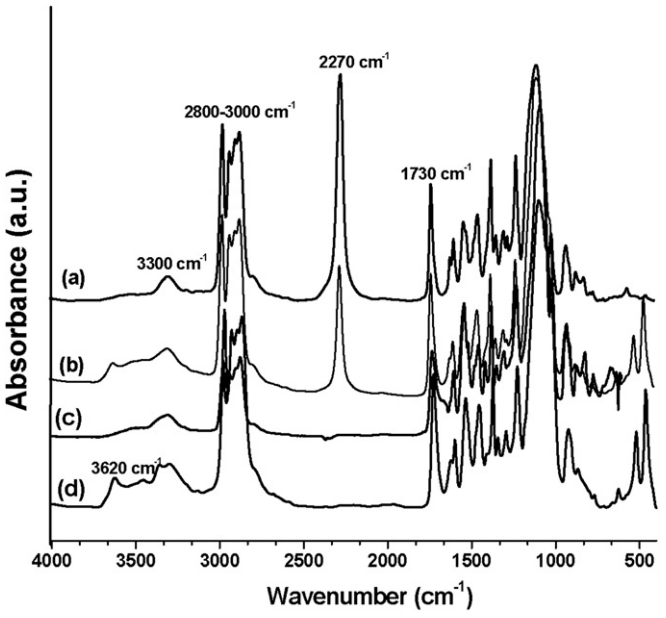

Fig. 8. FTIR spectra of (a) prepolymer (b) prepolymer with 8 wt% of clay (c) PU_{30} and (d) $PU_{30}CB_8$.

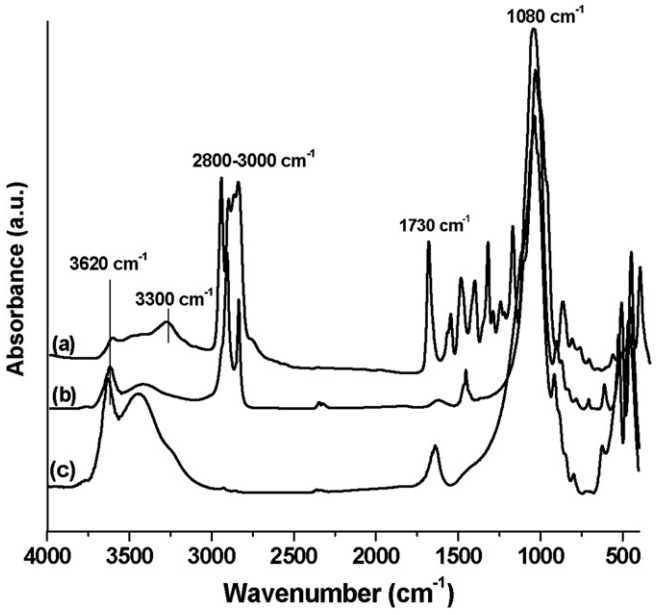

Fig. 9. FTIR spectra of Soxhlet extracted residues of composites with 8 wt% clay (a) $PU_{30}CB_8$ and (b) $PU_{30}CA_8$ and (c) $PU_{30}NA_8$.

polyurethane chains is associated with the residue of $PU_{30}CB_8$. It is seen from the FTIR spectra in Fig. 9a that the residue with Cloisite 30B has the characteristic peaks at 1731 cm^{-1} (carbonyl urethane stretching), 1526 cm^{-1} (C–NH– vibration), 1223 cm^{-1} (coupled C–N and C–O stretching), 1079 cm^{-1} (C–O stretching), 522 cm^{-1} (Al–O–Si deformation), and 1047 cm^{-1} (Si–O in plane stretching), indicating the presence of polyurethane chains and the clay particles in the residue. This clearly suggests that the $–CH_2CH_2OH$ groups in the surfactant of Cloisite 30B participate in the reaction. Fig. 9b, c for non-reactive clays (Cloisite Na and Cloisite 15A), however, show only the prominent Si–O stretching of the clay, indicating non-reactivity with the polyurethane chains. Some polymer chain ends with –NCO groups come closer to the vicinity of the clay galleries during the nanocomposites preparation and react with $–CH_2CH_2OH$ group of the quaternary ammonium ions to produce urethane linkage, –CO–NH–, leading to a fine dispersion of the clay particles, as seen in the TEM image discussed later. Non-permeable platy particles act as a barrier in gas diffusion by increasing the tortuosity of the diffusion path way.

With increase of addition of Cloisite 30B clay, more crosslinking occurs in the polyurethane network due to presence of –OH functional groups in the clay modifier. As we have discussed earlier in the FTIR section, the $–CH_2CH_2OH$ groups of the clay modifiers have a strong tendency to react with the –NCO groups of the prepolymer. There is a little change in crosslink density for Cloisite Na and Cloisite 15A clay nanocomposites as compared to that of the pristine PU (M_c values of $PU_{30}CB_0$, $PU_{30}NA_8$ and $PU_{30}CA_8$ are 4665, 4649 and 4610 g/mol respectively).

Introduction of the inorganic materials has clear effect on the gas permeability. In general, the gas permeability of the PU nanocomposites is lower than that of neat PU. This behavior could be attributed to presence of high aspect ratio and rigid platelets of clay in the polymer matrix. The crosslink density is important when there is no clay in the PU matrix, but in the presence of clay, both

Table 2
Summary of the different models for the gas permeation.

Model	Filler type	Particle geometry	Formula
Nielsen [31]	Ribbon	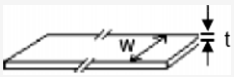	$R_p = \frac{1-\phi}{1+\alpha\phi/2}$
Cussler-regular array [32]	Ribbon	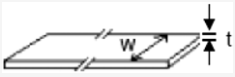	$R_p = \frac{1-\phi}{1+\alpha^2\phi^2/4}$
Maiti and Bhowmick [33]	Ribbon	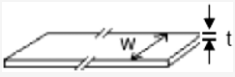	$R_p = \frac{1-\phi}{(1+\alpha\phi/2)^2}$
Cussler-random array [32]	Ribbon	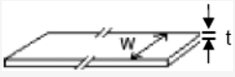	$R_p = \frac{1-\phi}{(1+\alpha\phi/3)^2}$
Gusev-Lusti [34]	Disk	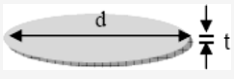	$R_p = \frac{1-\phi}{\exp[(\alpha\phi/3.47)^{0.71}]}$
Fredrickson-Bicerano [35]	Disk	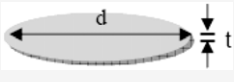	$R_p = \frac{1-\phi}{4[(1+x+0.1245x^2)/(2+x)]^2}$ Where, $x = \frac{\pi\alpha\phi}{2\ln\alpha/2}$
Bharadwaj [36]	Ribbon	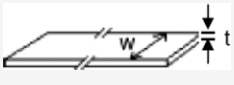	$R_p = \frac{1-\phi}{1+\alpha\phi(2S+1)/6}$ Where, $S = (3\cos^2\theta - 1)/2$ (θ is the angle between the direction of penetrant flow and normal of the layer)

N.B.: α is the aspect ratio of the filler, Φ is the volume fraction of the filler and $R_p$is the relative permeability.

crosslink density and the dispersion of clay are important. Also, $-CH_2CH_2OH$ groups that are present on the Cloisite 30B help dispersion of the clay in the PU matrix by interaction with the –NCO groups present in the PU prepolymer leading to higher crosslink density. Interestingly, we have seen the improved gas barrier property with Cloisite 30B clay only, with higher crosslink density.

3.3. Modeling

When the layered silicate is fully exfoliated in the polymer matrix, greatly reduced gas permeability can be achieved. In order to reduce the gas permeability of PU nanocomposites, it is important to fully exfoliate the silicate layers into the PU matrix. Based on the tortuous path theory, the relative permeability can be generally expressed by following equation [26–28]:

$$R_p = \frac{P}{P_0} = \frac{1-\phi}{\tau} \tag{4}$$

where R_p is relative permeability; P is the permeability coefficient of the polymer nanocomposites; P_0 is the permeability coefficient of the neat polymer; φ is nanoplatelet loading level (in volume %); and τ is the tortuosity factor. Tortuosity factor have been calculated based on different models adopted by different theories. The ribbon and disk like shapes of nanoclay have been considered in this study. Sun et al. [26] tabulated most of theories for permeability model equations. The brief descriptions of the theories are tabulated in Table 2. Fig. 3 shows the experimental value of relative permeability of the three different nanocomposites with varying levels of clay, as compared to the theoretical prediction. The incorporation of the nanoclay particles decreases the helium permeability. As the level of clay loading is increased, the corresponding nanocomposites exhibit enhanced barrier properties, as discussed earlier.

It is necessary to understand the accurate aspect ratio of clay to compare our results with different models. It is not easy to determine the aspect ratio of aluminosilicate nanocomposites. TEM photographs at different magnifications are required to analyze the aspect ratio. Fornes and Paul [29] have described a detailed procedure for determination of aspect ratio of clay platelets in Nylon6/clay nanocomposites. Moreover, the aspect ratio may change during the processing [30]. The determination of aspect ratio has been done by Fornes and Paul method [29,30] in this investigation. Particle length analyses were performed using Scion Image for Windows (Beta 4.03). The following steps have been taken to prepare the data for analysis: (i) a bright field TEM image was obtained with even illumination. Images were chosen to be as representative of the bulk sample as possible; (ii) a photographic negative of the image was then scanned into a computer using flatbed transparency scanner (1200 dpi, 8-bit grayscale) and saved as a TIFF file; (iii) using Adobe PhotoshopTM, the contrast/brightness and channel curves were adjusted so that the particles stood out clearly from the background. Note that the best results were typically obtained when the image contrast was high and minimal image processing was required. After having set the scale and the threshold (the threshold was set to a uniform value for the whole image) in the images, the "Analyze Particles" feature was used to generate a table of particle. This table was then exported into Microsoft Excel, where histograms, statistical analysis, and histogram plotting were performed.

Fig. 10 shows a typical TEM image of a representative nanocomposite ($PU_{20}CB_2$) and its corresponding processed TIFF image. In general a much larger area is scanned than shown in Fig. 10. The data obtained in Fig. 11 are used to estimate the aspect ratio of the clay as defined by

$$\text{Aspect ratio of clay}(\alpha) = \frac{l}{t_1} \tag{5}$$

where l is the average particle length and t_1 is the average particle thickness. The basic nature of all other samples is same when compared with the samples in Figs. 10 and 11. The histogram plot shows the average value of length is 158.5 nm. The thickness calculated is 1.62 nm. Thus, the average aspect ratio of clay is 98. We have also calculated the aspect ratio by taking individual clay length and thickness. The aspect ratio is found to be 96 by taking

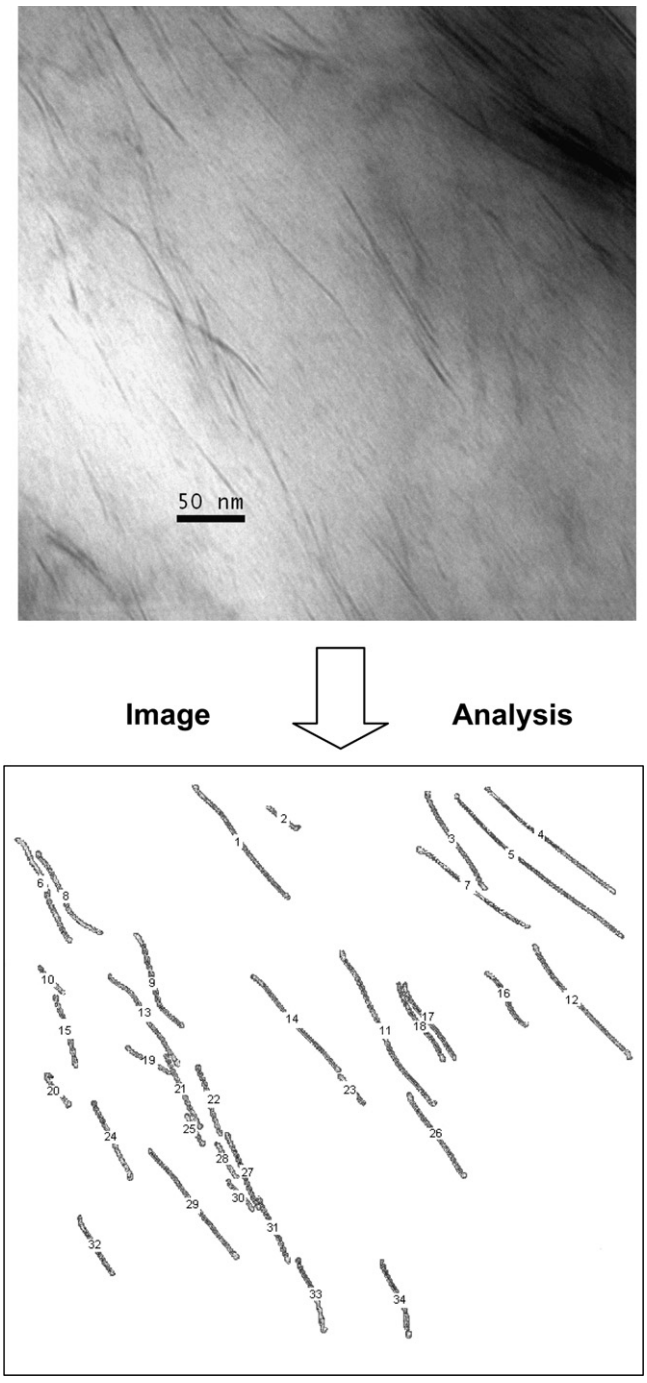

Fig. 10. Example of semi-automated analysis TEM image of representative sample [cured by 2nd generation hyperbranched polyol containing 2 wt% Cloisite 30B clay loading ($PU_{20}CB_2$)] for determining dispersed particle length of PU nanocomposites.

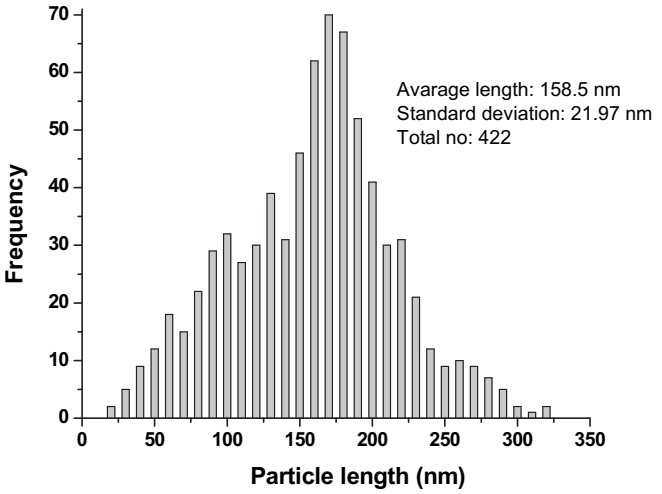

Fig. 11. Histogram of nanoclay particle length for PU nanocomposites after image analysis of representative sample [cured by 2nd generation hyperbranched polyol containing 2 wt% Cloisite 30B clay loading ($PU_{20}CB_2$)].

into account the average of about 100 individual clay layers for each sample. The results are almost similar in both the methods used for the determination of aspect ratio. It may be noted that the aspect ratio in the present investigation is higher than that reported by Forners and Paul [29], and Forners et al. [30], as they have used melt mixing while we have solution mixing. During the melt mixing, there is a probability of breakdown of the particles. Also, the clays used in the present investigation are different.

Below the filler loading of 8 wt%, the relative permeability value of the nanocomposites show good agreement with the Gusev-Lusti, the Nielsen and the Cussler (regular array) models. Interestingly, as the nanoparticles concentration is increased to a certain level, the nanoparticles tend to orient among themselves due to space constraining effect of the neighboring nanoparticles. As shown in the transmission electron microscopy photograph (Figs. 4 and 5), the clay particles do exhibit high level of orientation up to 8 wt% clay loading. Above 8 wt% loading of clay, the clay platelets are stacked to each other leading to agglomeration of nanoparticles. This is probably the reason why the experimental data do not match with the models above the 8 wt% of loading. Because of non dispersion and agglomeration of local nanoparticles, the experimental data significantly deviate above 8 wt% loading from the models. The relative permeability of $PU_{20}CB_8$ is 0.36 which is higher than the G-L model or the Nielsen model. This is because of the orientation of the nanoparticles.

4. Conclusions

In summary, we have demonstrated a facile route for the preparation of PU nanocomposite with novel architectures for high gas barrier property. PU cured with hyperbranched polyols exerts reasonable reduction in the helium penetration rate due to the higher crosslinking density of the matrix (~80% decrease from linear to 4th generation hyperbranched PU) and smaller domain size. Furthermore, the presence of small concentration of nanoclay (Cloisite 30B) platelets in the highly crosslinked PU further reduces the helium penetration rate to a greater extent by creating torturous paths for the gas molecules. There is ~76% decrease in permeability for 8 wt% Cloisite 30B filled PU over the control pristine 3rd generation PU. It has been shown that there is a good correlation between the morphology of PU generated and barrier properties. Among the clays, only Cloisite 30B demonstrates the best results. FTIR spectra confirm the interaction between the polyurethane matrix and Cloisite 30B clay. The permeation results have been compared with the different permeability models. The results are in good accord with the prediction by the Gusev-Lusti, the Nielsen and the Cussler (regular array) models at lower concentration of clay. It can be understood very clearly that the incorporation of nanoclays in a polymer matrix having tailor-made dendritic architecture will result in novel polymeric materials suitable for high end barrier applications.

Acknowledgement

The financial support of this work by Indian Space Research Organization, India is gratefully acknowledged.

References

[1] Findley BC, Johnson WS. In: Proceedings of the 44th AIAA/ASME SiD & M conference; April 2003.
[2] Humpenoder J. Cryogenics 1998;38:143–7.
[3] Hopfenberg HB. Permeability of plastic films and coatings to gases. NY: Plenum Press; 1974.
[4] Majumdar PS, Bhowmick AK, Majali AB, Tikku VK. J Appl Polym Sci 2000;75:784–95.
[5] Bohining M, Hao N, Schonhals A. Desalination 2006;200:142–3.
[6] Pu G, Longo ML, Borden MA. J Am Chem Soc 2005;127:6524–5.
[7] Bharadwaj RK, Mehrabi AR, Hamilton C, Trujillo C, Murga M, Fan R, et al. Polymer 2002;43:3699–705.
[8] Ulbricht M. Polymer 2006;47:2217–62.
[9] Osman MA, Mittal V, Morbidelli M, Ulrich W, Suter UW. Macromolecules 2003;36:9851–8.
[10] Damian C, Espuche E, Escoubes M, Cuney S, Pascault JP. J Appl Polym Sci 1997;65:2579–87.
[11] Xu R, Manias E, Snyder AJ, Runt J. J Biomed Mater Res 2003;64A:114–9.
[12] Yang JP, Chen ZK, Yang G, Fu SY, Ye L. Polymer 2008;49:3168–75.
[13] Puskas JE, Kwon Y, Antony P, Bhowmick AK. J Polym Sci Part A Polym Chem 2005;43:1811–26.
[14] Maji PK, Guchhait PK, Bhowmick AK. ACS Appl Mater Interfaces 2009;1:289–300.
[15] Maji PK, Bhowmick AK. J Polym Sci Part A Polym Chem 2009;47:731–45.
[16] Cao F, Jana SC. Polymer 2007;48:3790–800.
[17] Paul DR, Robeson LM. Polymer 2008;49:3187–204.
[18] Ganguly A, Bhowmick AK, Li Y. Macromolecules 2008;41:6246–53.
[19] Xu B, Zheng Q, Song Y, Shangguan Y. Polymer 2006;47:2904–10.
[20] Choudalakis G, Gotsis AD. Eur Polym J 2009;45:967–84.
[21] Flory PJ, Rehner JH. J Chem Phys 1943;11:521–30.
[22] ASTM D1434. American society for testing and materials. West Conshohocken, PA; 1982.
[23] Schapman F, Couvercelle JP, Bunel C. Eur Polym Mater 2002;38:1979–86.
[24] Burel F, Feldman A, Bunel C. Polymer 2005;46:15–25.
[25] Pattanayak A, Jana SC. Polymer 2005;46:3275–88.
[26] Sun L, Boo WJ, Clearfield A, Sue HJ, Pham HQ. J Memb Sci 2008;318:129–36.
[27] Takahashi S, Goldberg HA, Feeney CA, Karim DP, Farrell M, O'Leary K, et al. Polymer 2006;47:3083–93.
[28] Picard E, Vermogen A, Gerard JF, Espuche E. J Memb Sci 2007;292:33–144.
[29] Fornes TD, Paul RD. Polymer 2003;44:4993–5013.
[30] Fornes TD, Hunter DL, Paul DR. Polymer 2004;45:2321–31.
[31] Nielsen LE. J Macromol Sci A 1967;1:929–42.
[32] Lape NK, Nuxoll EE, Cussler EL. J Memb Sci 2004;236:29–37.
[33] Maiti M, Bhowmick AK. J Appl Polym Sci 2007;105:435–45.
[34] Gusev AA, Lusti HR. Adv Mater 2001;13:1641–3.
[35] Fredrickson GH, Bicerano J. J Chem Phys 1999;110:2181–8.
[36] Bharadwaj RK. Macromolecules 2001;34:9189–92.